Chemical Geology 511 (2019) 212–224

Contents lists available at ScienceDirect

Chemical Geology

journal homepage: www.elsevier.com/locate/chemgeo

Cycles of trace elements and isotopes in the ocean – GEOTRACES and beyond

Trace element concentrations, elemental ratios, and enrichment factors observed in aerosol samples collected during the US GEOTRACES eastern Pacific Ocean transect (GP16)☆

Clifton S. Buck[a,*], Ana Aguilar-Islas[b], Christopher Marsay[a], David Kadko[c], William M. Landing[d]

[a] Department of Marine Science, Skidaway Institute of Oceanography, University of Georgia, 10 Ocean Science Circle, Savannah, GA 31411-1011, United States
[b] College of Fisheries and Ocean Sciences, University of Alaska Fairbanks, Fairbanks, AK 99775, United States
[c] Florida International University, Applied Research Center, 10555 West Flagler St., Miami, FL 33174, United States
[d] Department of Earth, Ocean, and Atmospheric Science, Florida State University, Tallahassee, FL 32306, United States

ARTICLE INFO

Editor: Catherine Chauvel

Keywords:
GEOTRACES
Atmospheric deposition
Trace elements

ABSTRACT

Atmospheric deposition is an important source of bioactive trace elements to the open ocean, but observations of this flux are sparse. Atmospheric deposition of aerosol iron is of particular interest as it can play an important role in supporting primary production in the global ocean, yet it represents a key uncertainty that hampers accurate numerical modeling of the marine iron cycle. We report concentrations of atmospheric trace elements from samples collected as part of the 2013 US GEOTRACES GP16 zonal transect of the eastern Pacific Ocean. The cruise transected a relatively dusty region which coincided with the Peruvian upwelling zone before entering the much less dusty region of the subtropical gyre. The aerosol chemical composition and elemental ratios indicate crustal sources for Al, Ti, V, Mn, and Fe while the analyses suggest that Cu, Cd, and Pb originate from anthropogenic emissions.

Dry deposition fluxes were calculated by applying characteristic deposition velocities based on the expected particle size associated with each element. Bulk deposition, which includes wet and dry deposition, was calculated using the inventory of ^{7}Be in the upper water column. Soluble aerosol iron flux estimates were compared with vertical iron fluxes within the water column to assess the relative importance of atmospheric deposition to the marine iron cycle in the region. Atmospheric deposition was insignificant relative to the upwelling input of iron in the areas near the continental sources but increased in relative importance seaward of the coastal upwelling zone even as the magnitude of deposition decreased away from the coast.

This article is part of a special issue entitled: "Cycles of trace elements and isotopes in the ocean – GEOTRACES and beyond" - edited by Tim M. Conway, Tristan Horner, Yves Plancherel, and Aridane G. González.

1. Introduction

The quantification of atmospheric aerosol deposition remains an elusive goal over vast areas of the open ocean. This flux represents a primary mechanism of direct input of bioavailable limiting nutrients such as iron to the euphotic zone in regions removed from coastal inputs. Determination of atmospheric flux from direct observations relies on shipboard sample collections in regions lacking adequate island-based sampling opportunities, which limits the spatial coverage of measurements. The ephemeral nature of aerosol transport reduces the opportunity for relatively short-duration field sampling campaigns to capture short-lived dust events. Alternative methods, including satellite observations and water-tracer methods able to cover broader swaths of the ocean and integrate over longer time scales, have their own significant limitations (Anderson et al., 2016). Global-scale atmospheric deposition models require "ground truthing" of their results and the variability in the model predictions of iron deposition contributes to the disagreement among global ocean biogeochemistry models (Tagliabue et al., 2016). The international GEOTRACES program has expanded the collection and analysis of atmospheric samples to fill in spatial gaps in these observations and provides the added benefit of concurrent measurements of trace elements from the entirety of the water column.

☆ This article is part of a special issue entitled: "Cycles of trace elements and isotopes in the ocean – GEOTRACES and beyond" - edited by Tim M. Conway, Tristan Horner, Yves Plancherel, and Aridane G. González.

* Corresponding author.
E-mail address: clifton.buck@skio.uga.edu (C.S. Buck).

https://doi.org/10.1016/j.chemgeo.2019.01.002
Received 25 May 2018; Received in revised form 6 December 2018; Accepted 7 January 2019
Available online 17 January 2019

The eastern South Pacific Ocean is notable for its under representation in the marine aerosol literature relative to more studied regions like the North Atlantic Ocean and North Pacific Ocean (Sholkovitz et al., 2012). The island-based stations of the Sea-Air Exchange (SEAREX) program did not include any locations east of 150°W (Duce, 1989) and earlier ship-based samplings were semi-quantitative in nature (Prospero and Bonatti, 1969). Few recent oceanographic cruises have collected samples in the region but Baker et al. (2016) have published dry deposition fluxes of soluble aerosol trace elements from a cruise off the South American coast, and Wagener et al. (2008) reported observations from the BIOSOPE program that sampled the open tropical Southeast Pacific and estimated bulk deposition dust fluxes of < 40 $\mu g\,m^{-2}d^{-1}$. Collections made as part of the US CLIVAR program's repeat hydrography line P16, which ran along 150°W across the South Pacific Ocean, produced dry deposition dust flux estimates as low as 1.5 $\mu g\,m^{-2}d^{-1}$ (Buck et al., 2013). Dust from the arid areas of Peru and Chile is the sole contributor to marine sediments in the region south of approximately 5°S and west of the Peru-Chile trench (Saukel et al., 2011). This same study reported evidence of aeolian dust in the marine sediments as far west as the Galapagos Rise near 95°W.

The US-GEOTRACES Eastern Pacific Zonal Transect (Moffett and German, 2018) covered approximately 8000 km along 10°–15°S (Fig. 1), a region expected to receive a gradient of atmospheric deposition fluxes. The cruise also crossed a productive upwelling region (Kadko, 2017) and an oxygen minimum zone. Dust deposition is predicted to be < 0.50 $g\,m^{-2}y^{-1}$ into waters immediately offshore of western South America and lower still over the open South Pacific (Jickells et al., 2005). The aerosols transported to this region may reflect inputs from high altitude, arid regions of South America (Briceño-Zuluaga et al., 2016; Prospero, 2002), urban areas (Kunkel et al., 2012), smelting and mining activity (Saltzman et al., 1986; Salvador et al., 2016), and biomass burning (Ulke et al., 2011). The Andes Mountain range deflects the prevailing wind patterns northward along the coast confining the aerosol plumes to the nearshore and creating the characteristic upwelling regime (Wood et al., 2011). In addition, seasonal winds known as *vientos Paracas* occur several times per year during the austral winter. These southeasterly winds can mobilize mineral dust and distribute the material over the Peruvian continental shelf (Briceño-Zuluaga et al., 2017).

The input of aerosol iron has received the most attention due to the critical role of iron in alleviating micronutrient stress in high-nitrate, low-chlorophyll waters due to its ubiquity in biologically required enzymes (Morel and Price, 2003), but other trace elements such as manganese, copper, and cadmium play biological roles as well (Twining and Baines, 2013). Previous work in the region measured elevated concentrations of dissolved manganese in surface waters and suggested the source may be atmospheric deposition (Vedamati et al., 2015). As outlined in (Tagliabue et al., 2017), recent studies stemming from the GEOTRACES program have quantified the contribution of aerosol-derived iron to the reservoir of dissolved iron in the tropical Atlantic Ocean (Conway and John, 2014). The tropical Atlantic, like the eastern South Pacific (Pinedo-Gonzalez et al., 2015), is characterized by nitrogen limitation and the input of aerosol iron can stimulate the growth of nitrogen-fixing organisms (Falkowski, 1997; Moore et al., 2013). In addition to lithogenic elements, elements from anthropogenic sources like copper and lead, and elements of mixed sources like vanadium and manganese could impact surface water biogeochemical cycles (Pinedo-Gonzalez et al., 2015). How best to assess aerosol fractional solubility remains uncertain but research efforts indicate that solubility is a function of aerosol provenance (Aguilar-Islas et al., 2010), particle size, and/or particle processing during atmospheric transport (Baker and Croot, 2010). Regional differences in the mineralogy of crustal material, potential acidic processing of aerosol particles, atmospheric transport pathways, and proximity to anthropogenic aerosol sources reinforce the need to collect samples in a variety of ocean basins and improve spatial coverage.

Here we present chemical composition data from aerosol samples collected from the eastern subtropical Pacific Ocean region during late 2013 in addition to trace element atmospheric deposition flux estimates calculated by two methods, one provides dry deposition estimates and the other bulk deposition estimates. The former method reflects estimates for only the time period for which samples are collected while the latter extends flux estimates to reflect flux over a seasonal time frame assuming constant aerosol ratios. In the case of iron, these estimates are placed in oceanographic context by comparing with vertical fluxes to the euphotic zone via upwelling and diffusive mixing. Ideally, deposition could be measured directly on seasonal and annual time scales but opportunities for these types of collections are limited by the few appropriate island-based sampling sites and by the short timescales provided by oceanographic research expeditions. We use the activity of ^{7}Be to estimate atmospheric deposition rates on longer time scales thereby improving our ability to resolve those rates beyond the timeframe of the cruise.

2. Methods

2.1. Sample collection

Aerosol samples were collected aboard the R/V *Thompson* during the 2013 US-GEOTRACES Eastern Pacific Zonal Transect (GP16; Fig. 1).

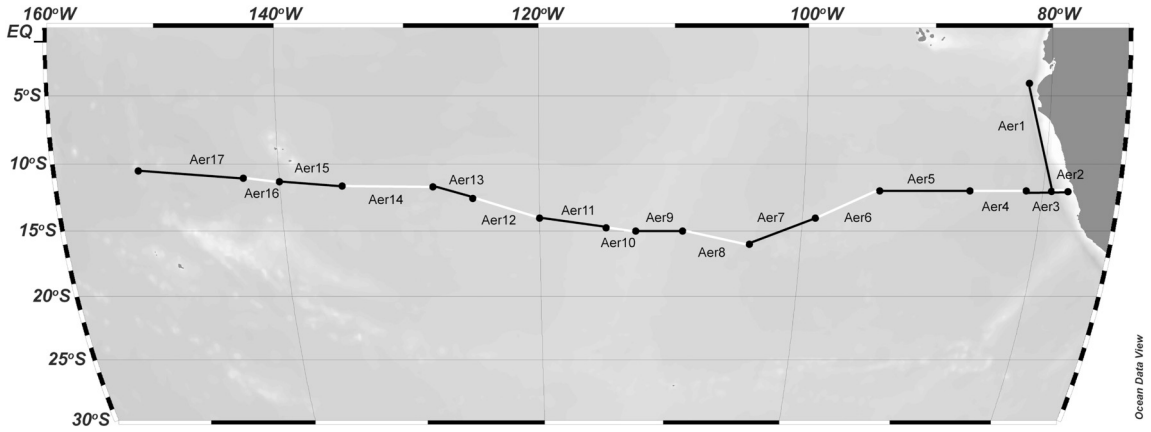

Fig. 1. The 2013 US GEOTRACES cruise track with aerosol sample deployment locations. Sampling began after leaving port in Manta, Ecuador and includes the transit south (Aer1) to the beginning of the westward cruise track. Recovery location of each sample coincides with deployment location of the next sample. Deployments are labeled chronologically; note the ship traveled from west to east during Aer2 and collection during Aer3 overlapped areas previously sampled during Aer1 and Aer2.

The ship sailed during October – December from South America to Tahiti in French Polynesia; a course which followed the prevailing wind pattern for the region. Bulk aerosol samples were collected on 12-replicate acid-washed 47 mm Whatman 41 (W41) ash-less filter discs mounted in Advantec-MFS polypropylene inline filter holders (PP47). Air was pumped through the filters using a high-volume aerosol sampler (model 5170V-BL, Tisch Environmental) capable of drawing approximately 100 L min^{-1} through each filter. The sampler was mounted on the starboard rail of the 03-deck approximately 16 m above sea level and forward of both the ship's superstructure and exhaust stacks. Other studies with this sampling system have used an automated sector-control system to provide power to the samplers only during times that wind conditions were optimal. For this study, the sector-control system was damaged by a power surge on the ship prior to the cruise. Thus, the aerosol samplers were controlled manually and only activated while the ship was on station with the bow pointed into the wind. This was done to prevent contamination from stack gases and ship operations. Sampling was not done while underway because under following winds the apparent wind speed was often zero or blowing faster than the ship's speed. Each sampling deployment lasted approximately three days producing 17 sets of aerosol samples (denoted as AerN hereafter). However, the mean sampling duration was shorter, 42.6 h with periods ranging from 32.0 to 61.4 h, because of periods when the wind was not optimal. The average amount of air passing through each filter was 231 m^3. The minimum volume of filtered air per filter was 165 m^3 and the maximum was 342 m^3 (Table 1).

2.2. Sample handling

All handling of aerosol filters was done inside a positive-pressure clean “bubble” constructed within the main laboratory area of the ship. Built of powder-free plastic sheeting, this controlled-access area was fed by several HEPA-blower units including one unit suspended directly above the aerosol group's work area. All work surfaces were covered with plastic sheeting. Pre-washed filters were stored in plastic petri dishes that were in turn stored double bagged inside a sealed storage box. All filter changes were done under the HEPA blower. Loaded filter holders were stored in sealed plastic bags until deployment. Recovered filters were returned to their petri dishes, double bagged, and then transferred to the ship's freezer.

2.3. Total aerosol trace element analysis and reference materials

Three replicate sample filters from each deployment were digested and analyzed for trace elements as described below. Deployment blanks (n = 3) and pre-cleaned filter blanks (n = 18) were digested and analyzed along with the samples. Averaged values from the 21 blank filter replicates were subtracted from each sample replicate. The average value from the three sample replicates, and the standard deviation of the replicates are reported in Table 2. Outliers (> 4σ from the mean) were not included in the average value. Samples with values lower than the blank are not reported. Total trace metal concentrations in the samples were determined at the University of Alaska Fairbanks by inductively couple plasma mass spectrometry (ICPMS) using a Thermo Element-2 ICP mass spectrometer. Quantification was done using external calibration curves generated from standard solutions in 1.6 M nitric acid. Samples were introduced directly into the Element-2 using a quartz cyclonic-spray chamber. Gallium was used as an internal standard for drift correction. Blank values and detection limits are reported in Table 2. We used a nominal air volume of 250 m^3 to calculate blank concentrations and the detection limit for the method. Agreement among triplicate sample digestions was in general better for samples collected near the coast (e.g., RSDs < 5% for Al) than samples collected offshore (e.g., RSDs as high as 48% for Al). The total aerosol trace element data are available as part of the GEOTRACES Intermediate Data Product 2017 (Schlitzer et al., 2018).

All sample handling took place under ISO-5 conditions. Filters were sequentially digested in tightly-capped Teflon-PFA vials (15-ml, Savillex) on a hot plate (150° C), using high-purity acids. During the first digestion step a mixture of concentrated HNO_3 (1.5 ml) and HF (0.5 ml) was heated for 24 h. The second step consisted of heating concentrated HNO_3 (1.0 ml) for 12 to 18 h. Solutions were taken down to dryness after each step. The sample was prepared for analysis by redissolving the residue in 1.6 M nitric acid and transferring (4 × 2.5 ml aliquots) the sample to a 30 ml LDPE bottle. Blanks and SRMs were prepared following the same digestion procedure.

Standard reference materials (SRMs) were digested following the same procedure (Table 3). Commercially available reference materials for marine particles HISS-1, MESS-3, BCR-414, and the 0–3 μm Arizona Test Dust (ATD) were digested using the method described above. The ATD batch used has ID#10738D (16 Sept. 2010). Previous interlaboratory analysis of ATD (Shelley et al., 2015) suggest ATD can be used as a reference material for atmospheric particles. The ATD batch used here differs from that used by Shelley et al. (2015).

2.4. ^{7}Be in the upper ocean and in aerosols

Water column samples were collected to calculate the inventory of

Table 1
Aerosol sampling metadata from the GP16 cruise. Air volume is the amount of air passed through each of 12 replicate filters.

Deployment	Start date	Start latitude	Start longitude	End date	End latitude	End longitude	Air volume
		°S	°W		°S	°W	m^3
Aer1	26-Oct	4.07	81.99	29-Oct	12.01	79.20	342.4
Aer2	29-Oct	12.01	79.20	1-Nov	12.05	77.66	252.9
Aer3	1-Nov	12.05	77.66	4-Nov	12.00	81.50	233.5
Aer4	4-Nov	12.00	81.50	7-Nov	12.00	86.50	224.2
Aer5	7-Nov	12.00	86.50	10-Nov	12.00	94.00	231.0
Aer6	10-Nov	12.00	94.00	13-Nov	14.00	99.00	244.1
Aer7	13-Nov	14.00	99.00	16-Nov	16.00	104.00	223.3
Aer8	16-Nov	16.00	104.00	19-Nov	15.00	109.19	233.7
Aer9	19-Nov	15.00	109.19	22-Nov	14.98	112.75	263.1
Aer10	22-Nov	14.99	112.75	25-Nov	14.77	115.00	200.4
Aer11	25-Nov	14.77	115.00	28-Nov	14.00	120.00	259.8
Aer12	28-Nov	14.00	120.00	1-Dec	12.54	125.00	221.9
Aer13	1-Dec	12.54	125.00	4-Dec	11.67	128.00	258.5
Aer14	4-Dec	11.67	128.00	7-Dec	11.60	135.00	164.7
Aer15	7-Dec	11.60	135.00	10-Dec	11.31	140.00	200.0
Aer16	10-Dec	11.31	140.00	13-Dec	11.03	142.95	184.6
Aer17	13-Dec	11.03	142.95	16-Dec	10.50	152.00	221.1

Table 2
Blank corrected concentrations of aerosol trace metals and aerosol ^{7}Be activities collected during the GP16 cruise. Filter blank values are the mean of 21 replicates normalized to a filtered air volume of 250 m^3. The digestion method level of detection (LOD) is calculated as 3 times the standard deviation of 18 replicate reagent blanks and normalized to 250 m^3 of air.

Deployment	^{7}Be	Al	Ti	V	Mn	Fe	Cu	Cd	Pb
	dpm m^{-3}	pmol m^{-3}	pmol m^{-3}	pmol m^{-3}	pmol m^{-3}	pmol m^{-3}	pmol m^{-3}	pmol m^{-3}	pmol m^{-3}
Filter blank		11 ± 14	2.9 ± 0.8	0.01 ± 0.02	0.13 ± 0.18	8 ± 15	0.09 ± 0.09	0.02 ± 0.03	0.53 ± 0.55
LOD		0.16	0.047	0.0005	0.016	0.65	0.017	0.003	0
Aer1	0.185 ± 0.019	1877 ± 101	60.6 ± 2.8	9.10 ± 0.35	12.54 ± 0.51	588 ± 25	7.79 ± 0.41	0.523 ± 0.036	0.612 ± 0.073
Aer2	0.305 ± 0.024	3224 ± 104	103.3 ± 3.2	13.48 ± 0.62	21.85 ± 0.39	1102 ± 30	15.55 ± 0.66	0.714 ± 0.025	0.686 ± 0.102
Aer3	0.337 ± 0.023	7679 ± 42	231.4 ± 3.3	20.05 ± 0.57	45.52 ± 0.49	2323 ± 22	31.92 ± 0.84	0.777 ± 0.052	3.89 ± 0.24
Aer4	0.167 ± 0.024	1601 ± 18	55.7 ± 1.1	3.70 ± 0.04	12.48 ± 0.45	620 ± 24	9.05 ± 0.62	0.107 ± 0.004	0.384 ± 0.049
Aer5	0.096 ± 0.024	400 ± 19	11.0 ± 5.3	0.499 ± 0.004	1.15 ± 0.02	56.1 ± 1.1	0.99 ± 0.10	0.024 ± 0.017	< Blank
Aer6	0.123 ± 0.025	94.4 ± 9.9	9.8 ± 0.7	0.152 ± 0.014	0.65 ± 0.17	46.5 ± 7.7	0.65 ± 0.06	0.018 ± 0.008	< Blank
Aer7	0.262 ± 0.024	104 ± 10	11.9 ± 0.9	0.334 ± 0.005	0.81 ± 0.09	50.2 ± 5.9	0.87 ± 0.22	0.020 ± 0.009	< Blank
Aer8	0.102 ± 0.028	132.1 ± 0.2	11.3 ± 0.5	0.188 ± 0.009	0.82 ± 0.15	57.3 ± 2.1	1.07 ± 0.42	< Blank	< Blank
Aer9	0.138 ± 0.019	128 ± 23	9.4 ± 1.2	0.250 ± 0.024	0.81 ± 0.09	52.5 ± 9.7	1.14 ± 0.10	0.027 ± 0.001	0.793
Aer10	0.113 ± 0.024	107 ± 16	8.6 ± 0.3	0.083 ± 0.008	0.32 ± 0.05	21.8 ± 1.4	0.80 ± 0.31	< Blank	< Blank
Aer11	0.097 ± 0.019	111 ± 34	16.0 ± 0.9	0.116 ± 0.004	0.54 ± 0.07	46.9 ± 7.7	1.19 ± 0.27	0.025	< Blank
Aer12	0.164 ± 0.042	151 ± 8	16.3 ± 2.2	0.122 ± 0.012	0.92 ± 0.22	67 ± 27	1.22 ± 0.19	0.072 ± 0.003	0.736 ± 0.091
Aer13	0.209 ± 0.033	152 ± 15	26.7 ± 7.8	0.342 ± 0.066	1.53 ± 0.60	114 ± 16	1.50 ± 0.20	0.032 ± 0.006	< Blank
Aer14	0.089 ± 0.030	118 ± 1	17.5 ± 0.6	0.417 ± 0.012	1.12 ± 0.71	55.6 ± 4.3	1.45 ± 0.20	0.107 ± 0.066	< Blank
Aer15	0.100 ± 0.029	161 ± 4	10.6 ± 0.6	0.343 ± 0.012	0.297 ± 0.013	25.2 ± 4.3	1.18 ± 0.09	0.019	< Blank
Aer16	0.163 ± 0.016	129 ± 62	15.9 ± 8.1	0.266 ± 0.126	0.84 ± 0.35	62 ± 25	0.71 ± 0.28	0.027	< Blank
Aer17	0.154 ± 0.015	240 ± 28	23.4 ± 3.4	0.522 ± 0.015	1.07 ± 0.09	76.4 ± 4.6	0.86 ± 0.11	0.017 ± 0.001	< Blank

^{7}Be in the surface ocean along the GP16 cruise track. The details of the sample collection and analysis procedures are available elsewhere (Kadko, 2017; Kadko et al., 2016; Kadko and Johns, 2011). Briefly, 400–700 L of water were pumped from selected depths into large plastic barrels on the ship's deck. Samples were pumped from the barrels through iron-impregnated acrylic fibers at ~10 L min^{-1} (Krishnaswami et al., 1972; Lal et al., 1988; Lee et al., 1991) with an extraction efficiency of 76–82%. The fibers were subsequently dried, ashed, and pressed into pellets. For the aerosol filters, ^{7}Be was analyzed by stacking three replicate filters in a petri dish (Kadko et al., 2016). Beryllium-7 was measured by a low-background germanium gamma detector by the gamma peak at 478 keV. Both pellet and aerosol filters configurations were calibrated with a commercially prepared mixed solution of known gamma activities.

2.5. Atmospheric flux estimation

We use two methods to estimate atmospheric deposition to the region; one method to estimate dry deposition and another method for bulk deposition. Both methods are a function of the observed aerosol trace element concentrations and produce flux estimates which are uncertain for other time periods. Bulk aerosol deposition is the sum of the dry deposition flux and wet deposition flux. Although GP16 encountered few precipitation events wet deposition could be significant, therefore the dry deposition flux should be considered a lower limit estimate of bulk deposition.

Dry deposition fluxes are calculated based on the concentration of aerosols in the atmosphere (C_{atmos}) and an appropriate deposition velocity (V_d) as shown in the following equation:

$$F_{dry} = C_{atmos} \times V_d \quad (1)$$

with the caveat that the choice of V_d may introduce uncertainty in the

Table 3
Three certified standard reference materials (SRM) and a consensus reference material were analyzed in triplicate to assess the accuracy and precision of the digestion and ICP-MS methods. The SRMs include two marine sediment materials (HISS-1 and MESS-3) and a biological material (BCR-414). The acronym ATD refers to Arizona Test Dust (Powder Technology Inc.)

SRM	Units	Al	Ti	V	Mn	Fe	Cu	Cd	Pb
HISS-1	μg g^{-1}	6050	762	6.19	61.6	2260	2.28	NA	2.93
StDev	μg g^{-1}	180	94	0.18	0.8	100	0.44	NA	0.03
Certified value	μg g^{-1}	7300	800	6.80	66.1	2500	2.29	0.02	3.13
StDev	μg g^{-1}	500	0	0.78	4.2	100	0.37	0.01	0.4
Percent recovery	%	83	95	91	93	90	100	NA	94
MESS-3	μg g^{-1}	91,170	4160	232	295	44,660	33.3	0.29	23.9
StDev	μg g^{-1}	4330	270	8.9	11.1	2240	1.5	0	0.76
Certified value	μg g^{-1}	85,900	4400	243	324	43,400	33.9	0.24	21.1
StDev	μg g^{-1}	2300	600	10	12	1100	1.6	0.01	0.7
Percent recovery	%	106	95	96	91	103	98	120	113
BCR-414	μg g^{-1}	2520	125	7.89	282	1880	30.1	0.4	3.88
StDev	μg g^{-1}	210	16	0.12	9	160	0.38	0.1	0.09
Certified value	μg g^{-1}	NA	NA	8.10	299	1850	29.5	0.38	3.97
StDev	μg g^{-1}	NA	NA	0.18	13	190	1.3	0.01	0.19
Percent recovery	%	NA	NA	97	94	102	102	103	98
ATD (PTI-ID:10738D)	μg g^{-1}	73,240	3492	81.9	1230	40,610	67.3	1.36	42.5
StDev	μg g^{-1}	799	43	2	130	474	3.1	0.01	0.82
Shelley et al. (2015)	μg g^{-1}	69,600	3220	72.7	764	33,600	NA	NA	NA
StDev	μg g^{-1}	1870	50	1.1	12	600	NA	NA	NA
Percent recovery	%	105	108	113	161	121	NA	NA	NA

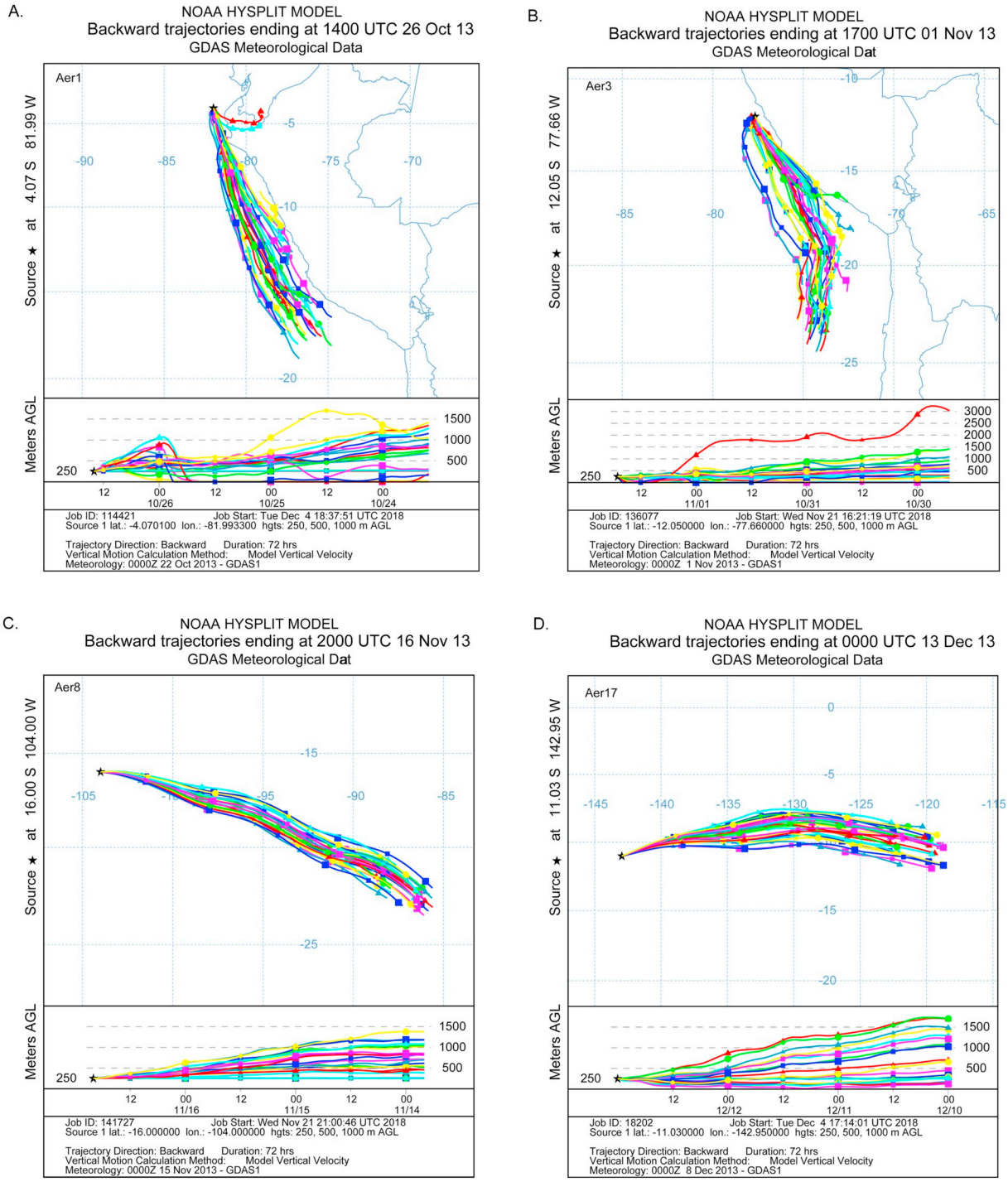

Fig. 2. Representative 3-day air mass back-trajectories (250 m starting height) from the starting deployment locations of (a) Aer1, (b) Aer3, (c) Aer8, and (d) Aer17 demonstrate the transition of atmospheric transport patterns from southeasterly to easterly as the ship followed the cruise track to the west. Trajectories for the other sampling periods are found in the Supplemental Information.

flux estimate as this term is sensitive to local meteorological conditions, e.g. wind speed and humidity, and is particle-size dependent (e.g. Buck et al., 2010; Chance et al., 2015; Duce et al., 1991). We have calculated fluxes for lithogenic elements (Al, Ti, V, Mn, Fe) assuming V_d equal to 1.16 cm s^{-1} (1000 m d^{-1}), a value consistent with dry deposition velocities for relatively large mineral dust particles (Duce et al., 1991). Fluxes of non-lithogenic elements (Cu, Cd, Pb) associated with smaller particles were calculated with V_d equal to 0.3 cm s^{-1} (260 m d^{-1}) (Chance et al., 2015). These deposition velocities are greater than applied in similar studies but are within expected uncertainties (e.g. Ellwood et al., 2018; Shelley et al., 2017)

Bulk deposition velocities can be estimated based on the upper ocean inventory of ^{7}Be (Kadko et al., 2016; Kadko et al., 2015). Beryllium-7 ($t_{1/2}$ = 53.3 d) is produced in the atmosphere by cosmic rays, deposited into the ocean, and subsequently homogenized in the mixed layer. In the absence of scavenging in typical low-particle ocean regimes the ^{7}Be inventory will represent an integration of the atmospheric deposition flux over the preceding 77 d mean life (e.g. Kadko and Johns, 2011). This region of the eastern Pacific Ocean is characterized by strong upwelling resulting in a dilution of the ^{7}Be

inventory in the surface mixed layer impacted by that upwelling (Kadko, 2017). Thus, we have corrected those inventories based on the inventory of the easternmost GEOTRACES hydrostation (Station 15) which was not significantly impacted by upwelling. The ^{7}Be data are available as part of the GEOTRACES Intermediate Data Product 2017 (Schlitzer et al., 2018).

The effective bulk deposition velocity (V_{Be}) is derived from the ratio of ^{7}Be flux (F_{Be}), equal to the ^{7}Be inventory multiplied by the ^{7}Be decay constant of 0.013 d^{-1}, to the activity of ^{7}Be (A_{Be}) in collected aerosols.

$$V_{Be} = F_{Be}/A_{Be} \quad (2)$$

We estimate the bulk flux for aerosol trace elements (F_{TE}) from the concentration of trace elements in the aerosols (C_{TE}) and V_{Be} by the equation:

$$F_{TE} = C_{TE} \times V_{Be} \quad (3)$$

This method was used to quantify atmospheric flux to the waters off Bermuda which compared well with fluxes derived from rain samples collected at the Bermuda Institute of Ocean Sciences Tudor Hill Marine Atmospheric Observatory (Kadko et al., 2015).

2.6. Air mass back trajectories

The NOAA Air Resources Laboratory Hybrid Single-Particle Lagrangian Integrated Trajectory (HySPLIT) model was used to simulate three-day (72 h) air mass back trajectories (AMBTs; Rolph et al., 2017; Stein et al., 2015). The Global Data Assimilation System (GDAS) provided the meteorology data set at a resolution of 1° latitude. The "ensemble" version of the model was run to provide multiple trajectories offset from the starting location by a fixed grid factor. This model type requires that the starting height for each model run be > 250 m above ground level. We chose starting heights of 250 m, 500 m, and 1000 m to assess the impact of variability in the model output caused by the marine boundary layer. Simulation runs were configured to originate at the temporal and spatial start, midpoint, and end of each sample collection period producing three unique AMBTs.

3. Results and discussion

3.1. Aerosol provenance

The aerosols of the eastern subtropical Pacific Ocean have received scant attention relative to dustier regions. We have used a combination of air mass back-trajectories (AMBTs) and aerosol elemental ratios to deduce aerosol source as this may be a primary factor dictating aerosol trace element fractional solubility (Aguilar-Islas et al., 2010; Buck et al., 2013; Sholkovitz et al., 2012). For the eastern-most deployments, prevailing southerly and southeasterly wind patterns transported air masses roughly parallel to the South American coast and few of the AMBT simulations showed an air mass to have passed over the continent (Fig. 2). These simulations downplay the potential for continental influences, but chemical indicators described below clearly show the impact of these sources on the samples collected during the cruise. A previous study which collected aerosols along the west coast of South America from 6.4°S to 15.5°S reported similar observations (Baker et al., 2016). As the ship moved west, the modeled AMBTs transitioned to follow the dominant easterly patterns characteristic of the trade winds.

The magnitude of aerosol trace element concentrations changed during the transition from southeasterly to easterly air mass transport patterns. During the first four sample deployments, covering a spatial range from 4°–12°S latitude and 77°–82°W longitude, aerosol Al concentrations ranged from 1601 to 7680 pmole m^{-3} (Fig. 3). The highest aerosol Al concentration of the cruise was measured during Aer3 which began at 12.05°S and 77.66°W and ended at 12.00°S and 81.50°W. Aerosol Al concentrations fell to an average of 156 pmole m^{-3} after Aer4 (west of 86.5°W; Fig. 3) indicating a transition from the relatively dusty region proximate to continental influences (Area 1) and the more pristine environment over the open ocean (Area 2). The former generally corresponds with the shelf and upwelling portion of the transect while the latter includes the oxygen minimum zone and gyre regimes (e.g. Black et al., 2018; Kadko, 2017). Aerosol Ti, also a useful tracer of lithogenic material, followed a similar pattern (Table 2, Supplementary Fig. 1). Concentrations of aerosol Ti were higher in the first four deployments relative to samples collected over the rest of the cruise and (similar to Al) the peak aerosol Ti concentration was collected during Aer3. After the change in atmospheric transport path, the concentrations of the lithogenic elements decreased by roughly a factor of ten. These observations suggest that atmospheric deposition should be most significant in the region of the Peruvian coastal upwelling (Kadko, 2017), which is characterized by high concentrations of macronutrients and high surface chlorophyll concentrations. Aerosol Pb showed a somewhat different pattern. Only six samples contained measurable concentrations of aerosol Pb; Aer1 — Aer4, Aer9, and Aer12. Of these six, the concentration measured for Aer3 was approximately a factor of six to eight higher than the other five samples. Earlier work during June – August 1982 generally agrees with the our observations of aerosol trace element concentration (Raemdonck et al., 1986). However, our study shows that aerosol Fe concentrations off of Peru were higher in 2013 than during 1982 while aerosol Cu and aerosol Pb were generally lower. Both datasets are only representative of short periods and we are unable to draw further conclusions about the variability of aerosol concentrations over that 30-year period.

Spearman's rank correlation analysis showed that all elements had statistically significant positive correlations except for Pb which lacked statistically significant associations (Table 4). Aluminum and Ti are strongly associated with mineral dust because of their abundance in the upper continental crust and these elements show correlations with Fe and Mn which are also considered crustal elements but may have anthropogenic sources as well. Aerosol V could be associated with heavy oil fly ash and has been shown to be a strong indicator of anthropogenic activity at Bermuda (Sholkovitz et al., 2012); however, V was more associated with Al, Ti, and Mn than with Cu, Cd, and Pb. This result might suggest that aerosol V is primarily a component of crustal material in this region rather than originating in anthropogenic emissions. Previous work reported a weak correlation between aerosol V and the concentration of marine organic matter further complicating the interpretation (Hawkins et al., 2010). Alternatively, correlations may indicate mixed provenance of aerosols collected offshore. The results of

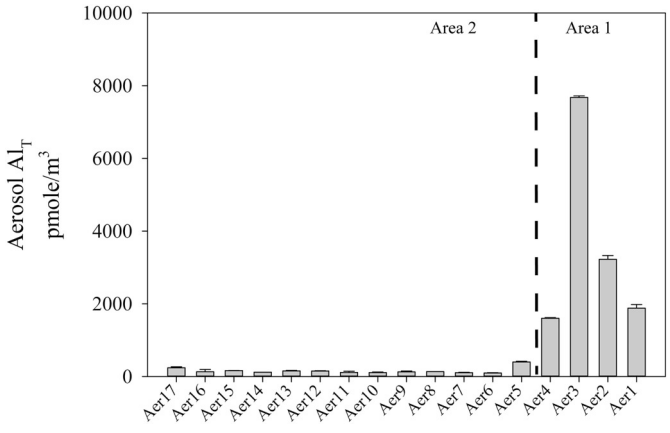

Fig. 3. Aerosol Al concentrations (pmole m^{-3}) from samples collected during the 2013 US GEOTRACES Eastern Pacific Zonal transect oriented from west to east. Error bars show ± 1 standard deviation of analyses on replicate samples. The dashed line indicates 86.5°W which is used as the demarcation between dusty (Area 1) and non-dusty areas (Area 2). Plots for the other aerosol trace elements reported in this study are shown in the supplemental material.

Table 4
Spearman's rank correlation matrix for aerosol trace elements collected during the GP16 cruise. Italic values represent correlation coefficients with *P* values > 0.050 which are not statistically significant.

	Al	Ti	V	Mn	Fe	Cu	Cd	Pb
Al	x	0.708	0.806	0.787	0.814	0.686	0.552	*0.086*
Ti		x	0.752	0.843	0.890	0.779	0.738	*0.086*
V			x	0.782	0.679	0.664	0.509	*0.143*
Mn				x	0.919	0.679	0.747	*0.086*
Fe					x	0.684	0.731	*0.029*
Cu						x	0.872	*0.029*
Cd							x	*0.086*
Pb								x

the statistical analysis are ambiguous for aerosol Cu because the correlations are similar between Cu and both crustal and anthropogenic elements. Previous work suggests that aerosol Cu may have been produced by the smelting facility in Ilo, Peru (Baker et al., 2016; Gidhagen et al., 2002). Of the statistically significant correlations, excluding aerosol Pb which showed no significant correlations, the relationships were weakest between Cd and the elements Al and V but stronger for the relationships of Cd with Ti, Mn, Fe, and Cu.

We used principal component analysis (PCA) to further investigate the relationships among the aerosol trace element concentrations. Aerosol Pb was excluded from the PCA because only six samples were greater than the level of detection and inclusion would have required culling of the total number of samples by two-thirds. The data from Aer8 and Aer10 were removed because the values of aerosol Cd were below the detection limit for these samples. The number of principal components (PC) was set to match the number of variables but only the results for the first three PCs are reported (Table 5). Most of the sample variance (> 97%) is explained by PC1 for all aerosol elements excluding aerosol Cd (~87%). The component loading plot for PC1 against PC2 (Supplemental Fig. 2) shows that Al, Ti, Mn, Fe, and Cu cluster together with nearly identical positive relationships between the two components. The aerosol Cu result is surprising given the expected sources from anthropogenic emissions in the region. Only Cd and V have negative correlations with PC2 and that component explains 12.9% and 2.3% of their respective variance. Principal Component 2 is unlikely to be contributions from anthropogenic emissions. Anthropogenic emissions associated with high-temperature industries like metal smelting are a source of aerosol Cd and this process produces Cd-enriched particles that are in the fine mode (< 1 μm) allowing for long-range transport (Bridgestock et al., 2017 and references therein), therefore aerosol Cd should have a positive correlation with an indicator of this process and aerosol Cu should be influenced as well. The PCA results suggest that aerosol V concentrations are largely controlled by mineral dust (PC1), but some other source or process (PC2) may have an impact. Thus, the results of the principal component analysis are ambiguous for some elements of interest in this study.

The chemical composition of the aerosols can be a useful indicator of aerosol provenance when constituent elements are normalized by crustal indicators such as the lithogenic elements Al and Ti. Aluminum is the more abundant element in crustal material but is not always the best choice. For example, aerosols from North Africa are depleted in Al relative to the upper continental crust (Shelley et al., 2015) and the elemental ratios of bulk continental crust may not be representative of those in South American crustal material as has been shown for Saharan soils (Guieu et al., 2002). Titanium has also been recommended as a lithogenic tracer in studies of water column particles (Ohnemus and Lam, 2015). Unfortunately, the chemical composition of the potential source material from South America is not well characterized. Because we do not have samples that are definitively characterized as coming from lithogenic sources by AMBT simulation or the color of the collected material, we compare the molar ratios of bulk upper continental crust (UCC) and average Andesitic crust (AC) (Taylor and McLennan, 1995) to the ratios of aerosol trace elements to aerosol Ti.

Table 5
The percentage of variance explained by the principal components.

	PC1	PC2	PC3
Al	98.519	1.178	0.047
Ti	98.058	1.426	0.441
V	97.524	2.285	0.004
Mn	99.316	0.536	0.109
Fe	99.093	0.834	0.037
Cu	98.845	0.912	0.146
Cd	86.989	12.945	0.009

Fig. 4 shows the molar ratios of the aerosol trace elements relative to aerosol Ti. The samples which were shown to bear a crustal signature more closely match the ratios in AC rather than UCC suggesting that the former may be the more appropriate reference ratio for aerosols in this region. In the first five deployments of GP16 the Al/Ti ratios were equal to those reported for AC indicating a crustal source. The ratios of Fe/Ti from the first four samples supported this observation as well. With increasing distance from continental sources, the ratios of crustal trace element to Ti decreased to relatively constant values less than the AC ratio. The observed Fe/Ti ratios are within the bounds of observations collected on a previous section cruise in the region (Maenhaut et al., 1983). Aerosol Mn, however, presented a different pattern. The Mn/Ti ratio was more indicative of UCC early in the cruise and showed enrichment relative to AC but approached the lower value for AC material in samples collected farther offshore. The anthropogenic or mixed-source elements V, Cu, Cd, and Pb were enriched in the early samples. The V/Ti decreased seaward indicating either a reduction in aerosol V with distance from potential source regions, the impact of a new source of Ti-rich aerosols, or some combination of the two factors. Aerosol Cu, Cd, and Pb (where concentrations were measurable) remained enriched relative to crustal material across the eastern Pacific. This persistent enrichment supports the long-range transport of fine aerosol material from high-temperature industrial emissions.

3.2. Enrichment factors

Another useful strategy to assess the impact of pollution on aerosols is to use the elemental molar ratios to calculate enrichment factors (EFs) relative to crustal material. This tool has the added benefit of enabling comparisons of chemical composition among aerosols from a variety of regions and sources. By normalizing the ratio of the aerosol trace metal to the concentration of aerosol Ti by the crustal ratio, we can assess the relative proportions of lithogenic and anthropogenic sources to the bulk aerosol sample. By convention, EFs > 10 characterize pollution impacted aerosols. Vanadium, Cd, and Pb can be enriched in aerosols which were produced by industrial processes such as metal smelting and the combustion of fossil fuels, while Fe and Mn, which are associated with lithogenic sources, may also be enriched in anthropogenic aerosols (Shelley et al., 2015 and references therein).

In general, the EFs relative to upper continental crust (UCC) were greater than those relative to Andesite crust (AC; Fig. 5). Only aerosol Pb exhibited the opposite relationship. Following the reasoning in the previous section, we will focus the discussion on enrichment factors relative to AC. The EFs for the crustal elements Ti and Fe were all < 10 and ranged from 0.2 to 1.0 and 0.2 to 1.1 respectively. Vanadium and Mn, which may have an anthropogenic component and be indicative of mixed sources, were not enriched relative to AC including the samples collected relatively near the continent which might be expected to bear a stronger anthropogenic signature. The EFs of aerosol V ranged from 0.2 to 4.4 and the EFs of aerosol Mn were between 0.1 and 1.1. These results support the notion that lithogenic material is the primary source for these trace elements despite the proximity of urban areas and industrial centers along the western coast of South America.

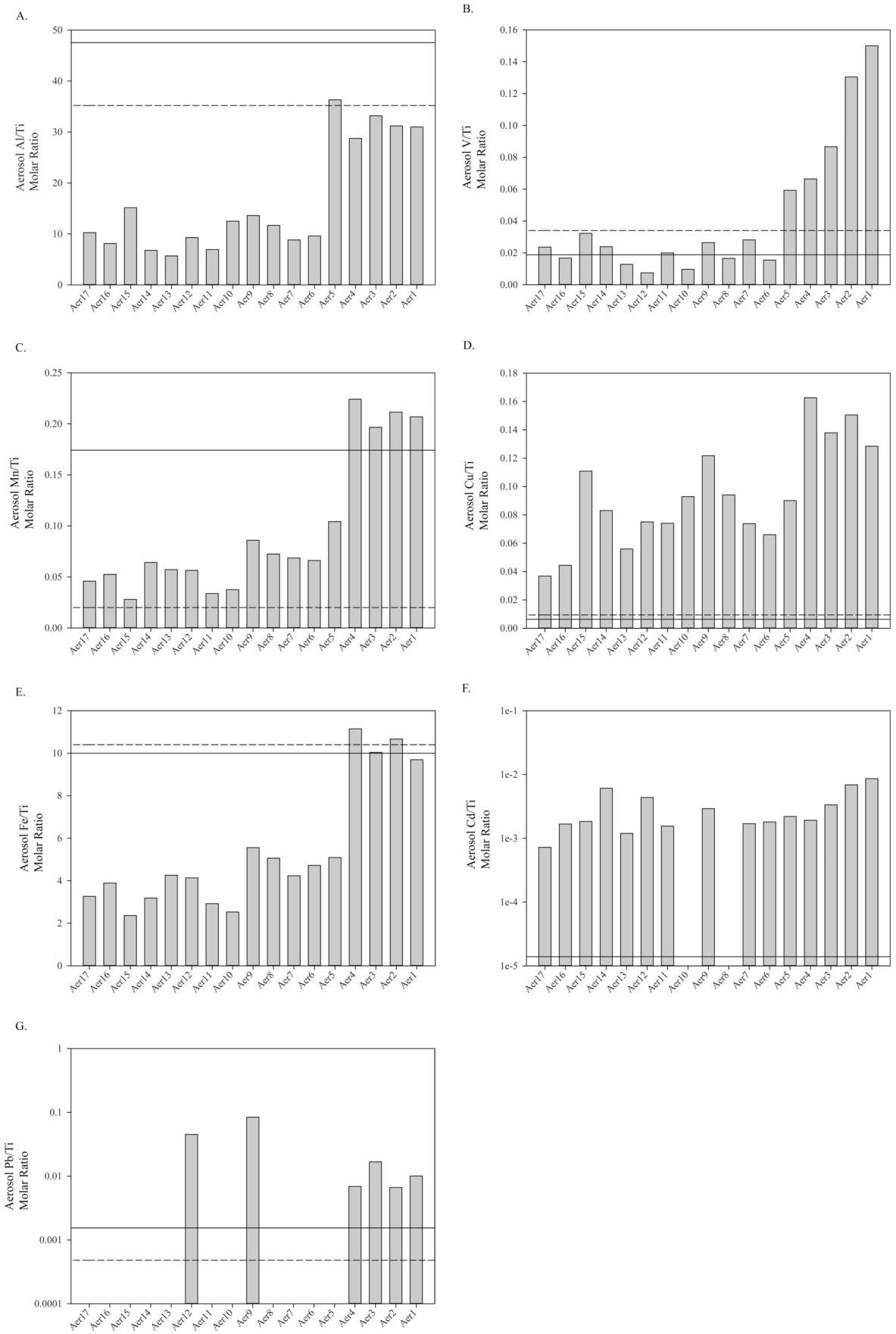

Fig. 4. Elemental ratios normalized to the concentration of aerosol Ti are plotted from west to east along the cruise track. For comparison, the ratio of upper continental crust (solid line) and average Andesitic crust (dashed line) are included (Taylor and McLennan, 1995).

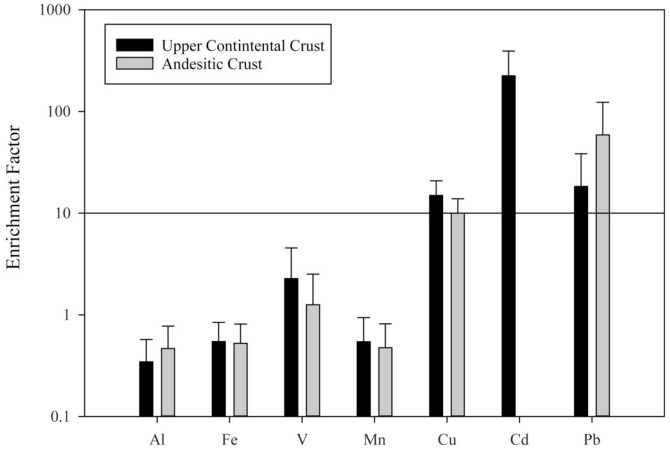

Fig. 5. Mean enrichment factors (± 1 standard deviation) calculated relative to the abundance of Ti in upper continental crust (dark bars) and average Andesitic crust (light bars). The average value of Cd is not reported by Taylor and McLennan (1995) for Andesitic crust. Enrichment factors > 10 (solid line) are considered to indicate pollution aerosol sources.

The trace elements enriched relative to AC (Cu and Pb) and UCC (Cd) were most likely associated with anthropogenic sources. Enrichment factors ranged from 3.9 to 17 for aerosol Cu, 52 to 620 for aerosol Cd, and 14 to 175 for aerosol Pb. The magnitude of the aerosol Cu EF changed after the first four deployments when aerosol concentrations became substantially lower. During the early deployments on the eastern end of the cruise section, the mean EF for Cu was 16 decreasing to a mean value of 8.3 for Aer5 – Aer17. The mean EF for aerosol Cd, calculated relative to UCC by necessity, also decreased between the groups of samples. The small number of aerosol Pb data ($n = 6$) limits our ability to interpret relationships among the anthropogenic-sourced trace elements as have been done by others. For example, aerosols in the tropical Atlantic Ocean showed a very strong correlation between EFs of aerosol Cd and aerosol Pb, relative to UCC (Rudnick and Gao, 2003), which was attributed to a common source process associated with the metal-smelting industry (Bridgestock et al., 2017). Our data did not show a significant correlation between EFs of aerosol Cd and aerosol Pb (or aerosol Cu) nor were EFs inversely related to aerosol Ti concentrations. The EFs for aerosol Cd for this cruise, relative to UCC, were also significantly higher than was reported for samples collected in the tropical Atlantic (Bridgestock et al., 2017). However, our EF values for Cd (calculated by mass ratio relative to UCC) were lower than those reported from the US-GEOTRACES cruise in the North Atlantic for samples attributed to marine air masses and were more consistent with samples attributed to European air masses (Shelley et al., 2015).

3.3. Atmospheric deposition flux

As noted above, dry deposition fluxes of crustal elements (Fig. 6a. Al, Fe; Fig. 6b. Ti, Mn, V) were calculated assuming a deposition velocity of 1.16 cm s^{-1} (1000 m d^{-1}) while flux estimates of non-crustal elements (Fig. 6c; Cu, Cd, Pb) assumed a deposition velocity of 0.3 cm s^{-1} (260 m d^{-1}). These estimates of dry deposition are strictly a function of aerosol concentration because the estimated deposition velocity is held constant, therefore the spatial pattern follows that which is shown in Fig. 3. The flux pattern of atmospheric aerosols to surface waters was characterized by relatively high rates in the shelf region of the cruise transect, as far west as 86.5°W, after which they decreased significantly. The estimated dry deposition fluxes of aerosol Al and aerosol Fe differed by about a factor of ten between dusty Area 1 and less dusty Area 2. This pattern was generally true for the other elements as well although the estimated flux rates were lower overall.

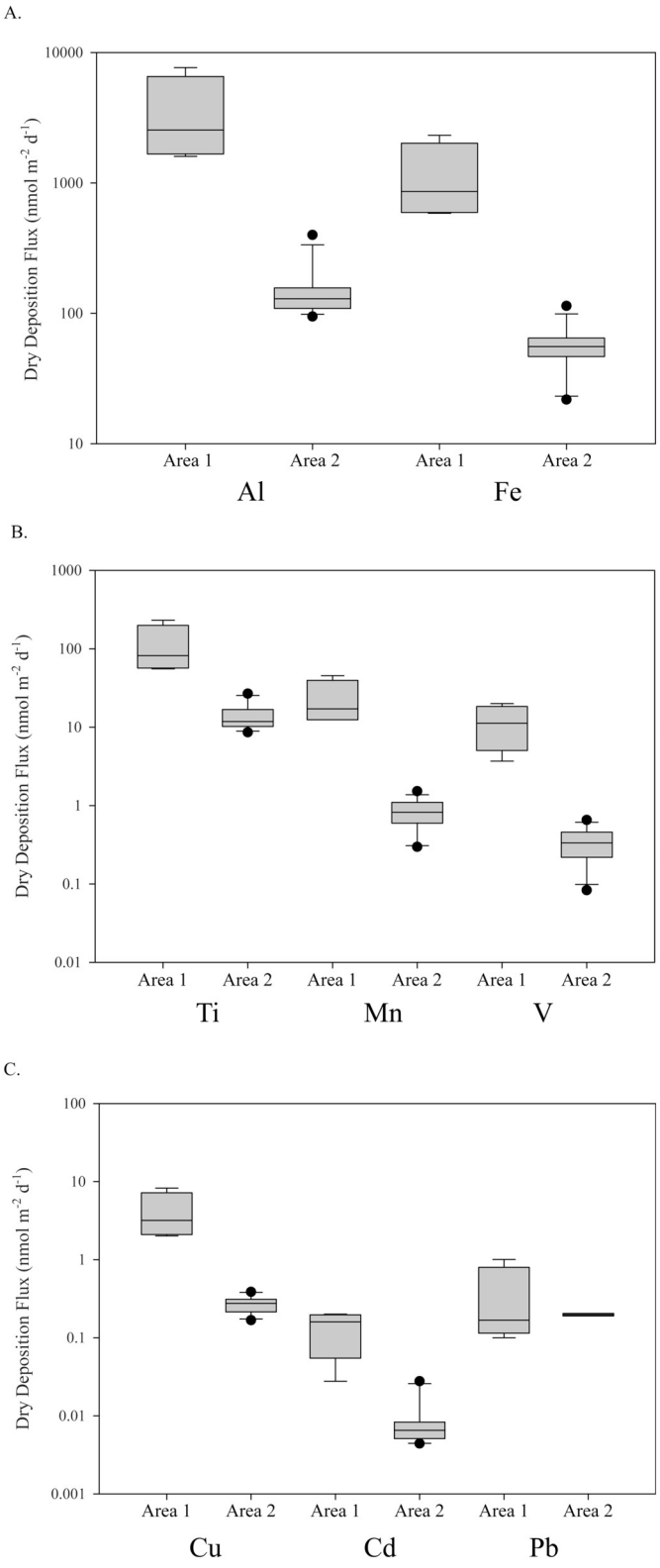

Fig. 6. Dry deposition fluxes of aerosol trace elements for Area 1 (east of 86.5°W) and Area 2 (west of 86.5°W). Panes (a) and (b) report the flux estimates for crustal elements based on a deposition velocity of 1.16 cm s^{-1} or 1000 m d^{-1}. Flux estimates in pane (c) are for non-crustal elements and are calculated with a deposition velocity of 0.3 cm s^{-1} or 260 m d^{-1}.

The daily accumulated precipitation product retrieved from NASA's Giovanni online environment indicate low precipitation rates for most of the cruise section during the period of August to December 2013

(TRMM_3B42_Daily v7, 0.25 deg). Precipitation rates were ~0.1 mm d^{-1} until Aer14 and then increased to 0.5 mm d^{-1}. Subsequently, precipitation rates rose to ~7 mm d^{-1} at the locations of Aer16 and Aer 17 (Supplemental Fig. 3). Decreasing surface salinity and an increasing ^{7}Be inventory are evidence of increasing precipitation as well (Fig. 7). This indicates that wet deposition should play a more significant role in atmospheric deposition as aerosols are transported to this region. Weather in French Polynesia during austral winter is characterized by heavy precipitation derived from the South Pacific Convergence Zone (SPCZ). The exact position of the SPCZ is dictated by the relative strength of the Kermadec high pressure system. As a result, atmospheric ^{7}Be activities can be low while the inventory in the upper ocean is enhanced due to washout (Heinrich and Pilon, 2013). We use the measured ^{7}Be inventory in the upper ocean to calculate the atmospheric flux of ^{7}Be thereby allowing a calculation of the bulk deposition velocity which captures the wet deposition input. Fig. 7 shows ^{7}Be inventories that have not been corrected for upwelling dilution (Kadko, 2017) but the correction has been applied to the inventory value used in the atmospheric flux calculation. The estimated ^{7}Be flux for upwelling stations east of Station 15 is held constant at 255 dpm $m^{-2}d^{-1}$, based on an inventory of 19,609 dpm m^{-2}, to match that of the non-upwelling station 15, then decreases by 40% at Station 18. Subsequently, the flux (and inventory) increases to the west, varying inversely with salinity (Fig. 7). The ^{7}Be flux to the upper ocean was highest in the waters of hydrostations 34 (10.77°S, 147.5°W) and 36 (10.50°S, 152.0°W) but no concurrent aerosol samples were collected at these locations.

Atmospheric transport is temporally and spatially sporadic such that variability in aerosol ^{7}Be activity (Table 2), rather than variability in the flux term calculated from the upper ocean inventory (Table 6), was the dominant driver of variability in V_{Be}. The results of the atmospheric deposition flux calculation can be smoothed by using a representative V_{Be} rather than the value derived from the "snapshot" aerosol observation. In this case, deposition velocities calculated from the ^{7}Be flux term and aerosol concentration (V_{Be}) had a mean value of 1500 ± 570 m d^{-1} (range: 835–2645 m d^{-1}); a range of values that is comparable to estimates in the North Atlantic (610–2800 m d^{-1}, Shelley et al., 2017). A comparison of the dry deposition flux estimate calculated with a constant V_d based on particle size and the average bulk deposition estimate derived from ^{7}Be shows that the latter is always greater than the former. We interpret this difference as the contribution of wet deposition to the bulk deposition estimate (Table 7). A comparison of the mean V_{Be} with the dry deposition velocities suggests that wet deposition may account for 30% and 80% of the total deposition respectively for crustal elements and non-crustal elements, based on our choice of dry deposition velocities for these particle populations. However, using the mean V_{Be} can introduce significant uncertainty in the flux calculation. For example, the aerosol trace element and ^{7}Be concentrations were highest for sample Aer3 but the corresponding upper ocean ^{7}Be inventory was not unusually high. The resulting calculated V_{Be} was only 756 m d^{-1}, half the mean of V_{Be} of 1500 m d^{-1} of all samples, leading to an estimate of trace element atmospheric fluxes half of that based on the mean value.

We can estimate a dry deposition flux for dust by assuming that the measured concentration of aerosol Al is solely derived from crustal material and that crustal material is 8.1% Al. These estimates range between 12 and 934 mg $m^{-2}y^{-1}$ (Table 7). The highest values are representative of the dustier Area 1. Only considering Area 2, the range of estimates narrows to 12–49 mg $m^{-2}y^{-1}$ with a mean value of 19 ± 10 mg $m^{-2}y^{-1}$. Total dust deposition estimates were 17–1401 mg $m^{-2}y^{-1}$ (assuming the mean V_{Be}) and 12–706 mg $m^{-2}y^{-1}$

Table 6
Measured ^{7}Be inventory from the upper ocean at select stations. Aerosol ^{7}Be fluxes are derived from the product of the ^{7}Be decay constant and the ^{7}Be inventories, except for stations 1–13 whose inventories are diluted by upwelling of deeper water (Kadko, 2017). These stations are assigned the inventory of the non-upwelling station 15. The deposition velocity (V_{Be}) values were calculated from the flux estimates and the observed aerosol ^{7}Be activities.

Station	Deployment	^{7}Be inventory	Aerosol ^{7}Be flux	V_{Be}
		dpm m^{-2}	dpm $m^{-2}d^{-1}$	m d^{-1}
	Aer1		254.9	1375
1	Aer2	5056	254.9	835
	Aer3		254.9	756
7	Aer4	10,043	254.9	1526
9	Aer5	13,072	254.9	2645
11	Aer6	16,991	254.9	2076
13	Aer7	18,598	254.9	972
15	Aer8	19,609	254.9	2489
	Aer9		202.8	1470
18	Aer10	11,590	150.7	1330
	Aer11		159.6	1641
23	Aer12	12,961	168.5	1028
	Aer13		178.4	853
26	Aer14	14,488	188.3	2127
	Aer15		191.1	1907
30	Aer16	14,906	193.8	1186
32	Aer17	18,258	237.4	1540
34		28,276	367.6	
36		36,546	475.1	

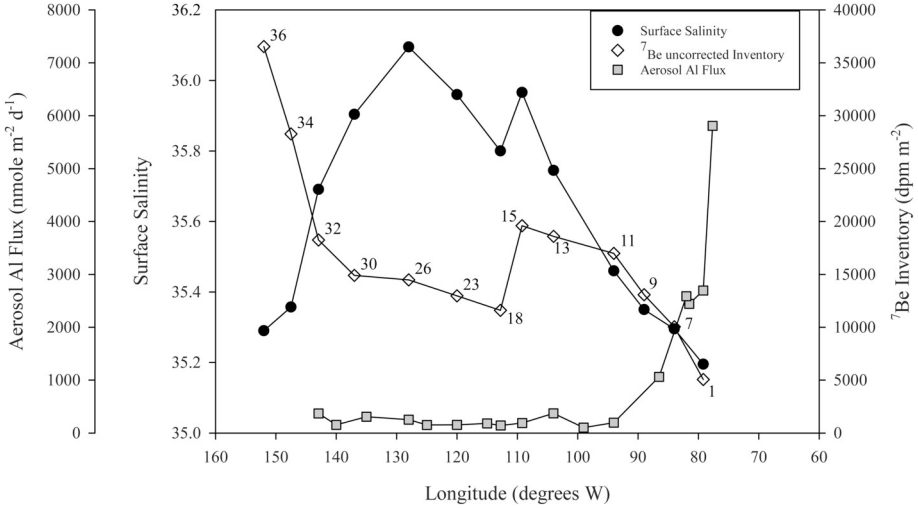

Fig. 7. Surface salinity and upper ocean ^{7}Be inventories plotted against longitude from the GP16 cruise. The aerosol Al flux was calculated using Eq. (3). Station numbers are indicated. The ^{7}Be inventories for eastern stations are not corrected for upwelling dilution (Kadko, 2017).

Table 7
The atmospheric fluxes of aerosol trace elements were estimated three ways and the data ranges are reported for each. Annual dust deposition was calculated from the flux of aerosol Al assuming that crustal material is 8.1% Al. [a]Flux calculated assuming a dry deposition velocity of 1000 m d^{-1}. [b]Flux calculated assuming a dry deposition velocity of 260 m d^{-1}. [c]Flux calculated using the mean estimated bulk deposition velocity of 1500 m d^{-1}. [d]Flux calculated using the estimated bulk deposition velocity from each aerosol deployment shown in Table 6.

	Units	Range of dry Deposition fluxes	Range of bulk Deposition fluxes[c]	Range of bulk Deposition fluxes[d]
Dust	mg m^{-2} y^{-1}	12 — 934	17 — 1401	12 — 706
Al	nmole $m^{-2}d^{-1}$	95 — 7679[a]	142 — 11,519	102 — 5808
Ti	nmole $m^{-2}d^{-1}$	8.6 — 231[a]	13 — 347	11 — 175
V	nmole $m^{-2}d^{-1}$	0.083 — 20[a]	0.12 — 30	0.11 — 15
Mn	nmole $m^{-2}d^{-1}$	0.30 — 46[a]	0.45 — 68	0.43 — 34
Fe	nmole $m^{-2}d^{-1}$	22 — 2323[a]	33 — 3485	29 — 1757
Cu	nmole $m^{-2}d^{-1}$	0.17 — 8.3[b]	0.97 — 48	0.84 — 24
Cd	nmole $m^{-2}d^{-1}$	0.004 — 0.20[b]	0.02 — 1.2	0.02 — 0.72
Pb	nmole $m^{-2}d^{-1}$	0.10 — 1.0[b]	0.58 — 5.8	0.57 — 2.9

(using the calculated V_{Be} for each sample). This flux trend corresponds with modeled deposition patterns for the region (Albani et al., 2014; Jickells et al., 2005).

3.4. Bioavailable iron fluxes to the surface ocean

This region of the Pacific is subject to a significant gradient in atmospheric deposition and is also characterized by two distinct oceanographic regimes, the upwelling zone and the oligotrophic gyre. The dustiest portion of the transect occurred coincidentally with GEOTRACES hydrostations located near the continental shelf and areas of significant upwelling. The less dusty samples were collected over the open ocean which is characterized by the strong stratification and oligotrophic conditions of the subtropical gyre.

In many regions of the world, the sediments of the continental shelf have proven to be important sources of dissolved trace elements to the open ocean (e.g. Charette et al., 2016; Lam and Bishop, 2008; Lam et al., 2006). Indeed, ^{228}Ra activity profiles from the GP16 transect indicate transport of sediment-influenced waters in the upper 200 m extending into the open ocean supplying 1.6×10^8 mol of dissolved Fe (dFe) per year to the shelf zone out to 90°W, although the dFe is not effectively transported off the shelf because of scavenging (Sanial et al., 2018). Assuming an aerosol Fe fractional solubility range of 1.5%–10%, we estimate the atmospheric deposition of soluble Fe (sFe_{atm}) to the shelf region (1.1×10^{11} m^2) to be significantly less, 0.55 to 3.7×10^6 mol y^{-1}, leading to the conclusion that dust deposition is a relatively minor source of potentially bioavailable iron to the Peruvian shelf.

Following the transect offshore, we assume that horizontal advection is not a significant source of dFe and that the inputs of bioavailable iron are dominated by vertical processes including upwelling, diffusive mixing, and atmospheric deposition. Following the principles described in Kadko (2017), we have calculated the upward dFe flux from upwelling and diffusive mixing as

$$F_{dFe} = w * [dFe]_c + K_z * (\delta [dFe]/\delta z)_c \quad (4)$$

where $[dFe]_c$ represents the dissolved Fe concentration at the base of the euphotic zone (John et al., 2018). The base of the euphotic zone, or particle production zone (PPZ), is defined as the water depth where chlorophyll fluorescence is 10% of the observed maximum (Ohnemus et al., 2017; Owens et al., 2015). Upwelling rates (w) and vertical diffusion coefficients (K_z) are shown in Table 8. K_z is approximated from ^{7}Be profiles using a one-dimensional advection-diffusion equation with a radioactive decay term (Kadko, 2017; Kadko and Johns, 2011). The estimated K_z values are similar to those reported from other areas of the Pacific Ocean (Ellwood et al., 2018; Haskell et al., 2015). Upwelling was a significant flux term up to hydrostation 15, but upwelling was not significant further west. For those stations vertical flux is calculated using an estimated vertical turbulent mixing coefficient (K_z) of 1.0×10^{-4} m^2 s^{-1}.

Aerosol deployments are grouped to correspond with the oceanographic setting where they were collected. The aerosol fluxes for Aer1 – Aer 7 were grouped as representative of deposition to the upwelling zone while Aer8 – Aer17 were associated with the region of the subtropical gyre. Estimated bulk (calculated from V_{Be}) and dry deposition fluxes (calculated with V_d = 1000 m d^{-1}) were averaged for the samples in those two groups and the results shown in Table 8. These estimates show that despite the relatively high fluxes offshore to ~104°W, atmospheric deposition is a minor factor in the cumulative flux of bioavailable iron to the surface ocean. The vigorous upwelling and significant turbulent vertical mixing bring approximately 1 μmole m^2d^{-1} of dFe into the surface ocean in the areas of most significant upwelling, seaward to 94°W. That input weakens significantly at hydrostations 11 and 15, yet the upward flux is still much greater than the downward atmospheric flux, which only accounts for about 1–2% of the total input of bioavailable Fe. The relative contribution of atmospheric deposition to the surface waters increases in the more stratified waters of the gyre. Upward flux is limited to turbulent mixing which supplies 0.8–6.4 nmol Fe $m^{-2}d^{-1}$ and is in fact a loss term at two of the stations. The deposition of sFe_{atm} from the atmosphere adds 1 to 6 nmol $m^{-2}d^{-1}$ based on assumed solubility for both flux estimates. This term can clearly be significant to the overall budget of bioavailable iron in the surface ocean of Area 2.

4. Conclusions

We have shown a sharp gradient in the concentration of marine boundary aerosols within approximately 7° of longitude moving west from the coast of South America and that the highest aerosol concentrations during the US-GEOTRACES GP16 transect occurred over the Peru upwelling zone region. Aerosol concentrations were low over the open ocean but were enriched in some elements (Cd, Cu, Pb) indicating an anthropogenic aerosol component. However, V did not show enrichment along the cruise track. Molar elemental ratios were more consistent with estimates in average Andesitic crust than in bulk upper continental crust, reinforcing the necessity to carefully consider the source material used to assess trace element enrichment. Our estimates show that atmospheric deposition is a minor source of bioavailable iron in the upwelling zone. Despite being located farther from the dust source, the surface ocean of the gyre is significantly impacted by aerosol deposition relative to inputs from vertical mixing processes. Other studies will report the fractional solubility of trace elements in these samples and data from size-fractionated samples. These studies will be crucial to assessing their potential importance as an input of biologically essential trace elements to the eastern Pacific Ocean.

Supplementary data to this article can be found online at https://doi.org/10.1016/j.chemgeo.2019.01.002.

Acknowledgements

We thank Chief Scientists Chris German and Jim Moffett for their support and the US GEOTRACES program for the opportunity to participate on this cruise. We also thank the Captain and crew of the RV *Thompson* for their expertise. Funding for this project was provided by the United States National Science Foundation through grants OCE-1454368 to CSB and WML, OCE-123279 to DK, and OCE-1234417 to AA. The authors gratefully acknowledge Dr. Mark Stephens for the ^{7}Be sample collection and analysis and the NOAA Air Resources Laboratory (ARL) for the provision of the HYSPLIT transport and dispersion model (http://www.ready.noaa.gov) used in this publication.

Table 8
Fluxes to the euphotic zone show a significant gradient moving offshore. The atmospheric fluxes of soluble aerosol Fe (sFe_{atm}) are estimated assuming a fractional solubility range of 1.5% — 10% for aerosol iron. The values shown are the mean flux for Aer1 — Aer7 (upwelling) and Aer8 — Aer17 (gyre). Bulk atmospheric deposition fluxes were calculated from the deposition velocity (V_{Be}) reported in Table 6. Dry deposition fluxes were calculated assuming a deposition velocity of 1000 m d^{-1}. The depths of the particle production zone (PPZ) base at each station were reported in Ohnemus et al. (2017). *Values reported in Kadko (2017) for stations 1–15. For stations 17–30, an estimate of 1.0×10^{-4} m^2 s^{-1} was used.

Regime	Station	Latitude	Longitude	PPZ depth	w*	K_z*	Upwelled Flux of dFe	Diffusive Flux of dFe	Bulk Atmospheric Flux of sFe_{atm}		Dry Atmospheric Flux of sFe_{atm}	
		S	W	m	m/d	$\times 10^{-4}$ m^2 s^{-1}	nmol $m^{-2}d^{-1}$	nmol $m^{-2}d^{-1}$	nmol $m^{-2}d^{-1}$		nmol $m^{-2}d^{-1}$	
									1.5 % Solubility	10% Solubility	1.5 % Solubility	10% Solubility
Upwelling	1	12.01	79.20	66	4.4	4.4	630	150				
	7	11.98	84.00	94	1.3	4.5	160	720				
	9	12.00	89.00	109	1.5	3.6	590	460	10.1 ± 9.3	67.6 ± 62.3	10.3 ± 12.4	68.4 ± 82.5
	11	12.00	94.00	130	0	1.7	2.9	50				
	15	16.00	104.0	168	0.2	3.0	14	110				
Gyre	17	15.00	109.2	163	0	1.0	0	1.4	1.3 ± 0.5	8.5 ± 3.5	0.9 ± 0.4	5.8 ± 2.6
	18	15.00	112.8	174	0	1.0	0	-11				
	20	15.00	113.5	191	0	1.0	0	3.5				
	21	14.77	115.0	167	0	1.0	0	2.4				
	23	14.00	120.0	169	0	1.0	0	4.5				
	25	12.54	125.0	163	0	1.0	0	6.4				
	26	11.67	128.0	169	0	1.0	0	0.8				
	28	11.63	132.5	162	0	1.0	0	1.8				
	30	11.58	137.0	138	0	1.0	0	-3.9				

References

Aguilar-Islas, A.M., Wu, J., Rember, R., Johansen, A.M., Shank, L.M., 2010. Dissolution of aerosol-derived iron in seawater: Leach solution chemistry, aerosol type, and colloidal iron fraction. Mar. Chem. 120 (1–4), 25–33.

Albani, S., et al., 2014. Improved dust representation in the community atmosphere model. J. Adv. Model. Earth Syst. 6 (3), 541–570.

Anderson, R.F., et al., 2016. How well can we quantify dust deposition to the ocean? Philos. Trans. R. Soc. A Math. Phys. Eng. Sci. 374 (2081), 26.

Baker, A.R., Croot, P.L., 2010. Atmospheric and marine controls on aerosol iron solubility in seawater. Mar. Chem. 120 (1–4), 4–13.

Baker, A.R., Thomas, M., Bange, H.W., Plasencia Sánchez, E., 2016. Soluble trace metals in aerosols over the tropical south-east Pacific offshore of Peru. Biogeosciences 13 (3), 817–825.

Black, E.E., Buesseler, K.O., Pike, S.M., Lam, P.J., 2018. 234Th as a tracer of particulate export and remineralization in the southeastern tropical Pacific. Mar. Chem. 201, 35–50.

Briceño-Zuluaga, F.J., et al., 2016. Terrigenous material supply to the Peruvian central continental shelf (Pisco, 14° S) during the last 1000 years: paleoclimatic implications. Clim. Past 12 (3), 787–798.

Briceño-Zuluaga, F., et al., 2017. Paracas dust storms: sources, trajectories and associated meteorological conditions. Atmos. Environ. 165, 99–110.

Bridgestock, L., et al., 2017. The Cd isotope composition of atmospheric aerosols from the Tropical Atlantic Ocean. Geophys. Res. Lett. 44 (6), 2932–2940.

Buck, C.S., Landing, W.M., Resing, J.A., Measures, C.I., 2010. The solubility and deposition of aerosol Fe and other trace elements in the North Atlantic Ocean: Observations from the A16N CLIVAR/CO2 repeat hydrography section. Mar. Chem. 120 (1–4), 57–70.

Buck, C.S., Landing, W.M., Resing, J., 2013. Pacific Ocean aerosols: Deposition and solubility of iron, aluminum, and other trace elements. Mar. Chem. 157, 117–130.

Chance, R., Jickells, T.D., Baker, A.R., 2015. Atmospheric trace metal concentrations, solubility and deposition fluxes in remote marine air over the south-east Atlantic. Mar. Chem. 177, 45–56.

Charette, M.A., et al., 2016. Coastal Ocean and shelf-sea biogeochemical cycling of trace elements and isotopes: lessons learned from GEOTRACES. Philos. Trans. R. Soc. A Math. Phys. Eng. Sci. 374 (2081), 20160076.

Conway, T.M., John, S.G., 2014. Quantification of dissolved iron sources to the North Atlantic Ocean. Nature 511 (7508) (212–+).

Duce, R.A., 1989. SEAREX: the sea-air exchange program. In: Riley, J.P.a.C., R. (Ed.), Chemical Oceanography. Academic Press, San Diego, CA, pp. 1–14.

Duce, R.A., et al., 1991. The atmospheric input of trace species to the world ocean. Glob. Biogeochem. Cycles 5 (3), 193–259.

Ellwood, M.J., et al., 2018. Insights into the biogeochemical cycling of iron, nitrate, and phosphate across a 5300 km South Pacific zonal section (153 degrees E-150 degrees W). Glob. Biogeochem. Cycles 32 (2), 187–207.

Falkowski, P.G., 1997. Evolution of the nitrogen cycle and its influence on the biological sequestration of CO2 in the ocean. Nature 387 (6630), 272–275.

Gidhagen, L., Kahelin, H., Schmidt-Thome, P., Johansson, C., 2002. Anthropogenic and natural levels of arsenic in PM10 in Central and Northern Chile. Atmos. Environ. 36, 3803–3817.

Guieu, C., Loye-Pilot, M.D., Ridame, C., Thomas, C., 2002. Chemical characterization of the Saharan dust end-member: some biogeochemical implications for the western Mediterranean Sea. J. Geophys. Res.-Atmos. 107 (D15), 11.

Haskell, W.Z., et al., 2015. Upwelling velocity and eddy diffusivity from 7Be measurements used to compare vertical nutrient flux to export POC flux in the Eastern Tropical South Pacific. Mar. Chem. 168, 140–150.

Hawkins, L.N., Russell, L.M., Covert, D.S., Quinn, P.K., Bates, T.S., 2010. Carboxylic acids, sulfates, and organosulfates in processed continental organic aerosol over the southeast Pacific Ocean during VOCALS-REx 2008. J. Geophys. Res. Atmos. 115 (13).

Heinrich, P., Pilon, R., 2013. Simulation of 210Pb and 7Be scavenging in the tropics by the LMDz general circulation model. Atmos. Res. 132–133, 490–505.

Jickells, T.D., et al., 2005. Global iron connections between desert dust, ocean biogeochemistry, and climate. Science 308 (5718), 67–71.

John, S.G., Helgoe, J., Townsend, E., Weber, T., DeVries, T., Tagliabue, A., Moore, K., Lam, P., Marsay, C.M., Till, C., 2018. Biogeochemical cycling of Fe and Fe stable isotopes in the Eastern Tropical South Pacific. Mar. Chem. 201, 66–76. https://doi.org/10.1016/j.marchem.2017.06.003.

Kadko, D., 2017. Upwelling and primary production during the US GEOTRACES East Pacific Zonal Transect. Glob. Biogeochem. Cycles 31 (2), 218–232.

Kadko, D., Johns, W., 2011. Inferring upwelling rates in the equatorial Atlantic using 7Be measurements in the upper ocean. Deep-Sea Res. I Oceanogr. Res. Pap. 58 (6), 647–657.

Kadko, D., Landing, W.M., Shelley, R.U., 2015. A novel tracer technique to quantify the atmospheric flux of trace elements to remote ocean regions. J. Geophys. Res. Oceans 120 (2), 848–858.

Kadko, D., Galfond, B., Landing, W.M., Shelley, R.U., 2016. Determining the pathways, fate, and flux of atmospherically derived trace elements in the Arctic ocean/ice system. Mar. Chem. 182, 38–50.

Krishnaswami, S., et al., 1972. Silicon, radium, thorium, and lead in seawater: In-situ extraction by synthetic fibre. Earth Planet. Sci. Lett. 16 (1), 84–90.

Kunkel, D., et al., 2012. Urban emission hot spots as sources for remote aerosol deposition. Geophysical Research Letters 39 (1) (n/a–n/a).

Lal, D., Chung, Y., Platt, T., Lee, T., 1988. Twin cosmogenic radiotracer studies of phosphorus recycling and chemical fluxes in the upper ocean. Limnol. Oceanogr. 33 (6), 1559–1567.

Lam, P.J., Bishop, J.K.B., 2008. The continental margin is a key source of iron to the HNLC North Pacific Ocean. Geophys. Res. Lett. 35 (7) (n/a–n/a).

Lam, P.J., et al., 2006. Wintertime phytoplankton bloom in the subarctic Pacific supported by continental margin iron. Glob. Biogeochem. Cycles 20 (1) (n/a–n/a).

Lee, T., Barg, E., Lal, D., 1991. Studies of vertical mixing in the southern California bight with cosmogenic radionuclides p-32 and BE-7. Limnol. Oceanogr. 36 (5), 1044–1053.

Maenhaut, W., Raemdonck, H., Selen, A., Van Grieken, R., Winchester, J.W., 1983. Characterization of the atmospheric aerosol over the eastern equatorial Pacific. J. Geophys. Res. Oceans 88 (C9), 5353–5364.

Moffett, J.W., German, C.R., 2018. The U.S.GEOTRACES Eastern Tropical Pacific Transect (GP16). Mar. Chem. 201, 1–5.

Moore, C.M., et al., 2013. Processes and patterns of oceanic nutrient limitation. Nat. Geosci. 6 (9), 701–710.

Morel, F.M., Price, N.M., 2003. The biogeochemical cycles of trace metals in the oceans. Science 300 (5621), 944–947.

Ohnemus, D.C., Lam, P.J., 2015. Cycling of lithogenic marine particles in the US

GEOTRACES North Atlantic transect. Deep-Sea Res. II Top. Stud. Oceanogr. 116, 283–302.
Ohnemus, D.C., et al., 2017. Elevated trace metal content of prokaryotic communities associated with marine oxygen deficient zones. Limnol. Oceanogr. 62 (1), 3–25.
Owens, S.A., Pike, S., Buesseler, K.O., 2015. Thorium-234 as a tracer of particle dynamics and upper ocean export in the Atlantic Ocean. Deep-Sea Res. II Top. Stud. Oceanogr. 116, 42–59.
Pinedo-Gonzalez, P., et al., 2015. Surface distribution of dissolved trace metals in the oligotrophic ocean and their influence on phytoplankton biomass and productivity. Glob. Biogeochem. Cycles 29 (10), 1763–1781.
Prospero, J.M., 2002. Environmental characterization of global sources of atmospheric soil dust identified with the NIMBUS 7 Total ozone Mapping Spectrometer (TOMS) absorbing aerosol product. Rev. Geophys. 40 (1).
Prospero, J.M., Bonatti, E., 1969. Continental dust in the atmosphere of the Eastern Equatorial Pacific. J. Geophys. Res. 74 (13), 3362–3371.
Raemdonck, H., Maenhaut, W., Andreae, M.O., 1986. Chemistry of marine aerosol over the tropical and equatorial Pacific. J. Geophys. Res.-Atmos. 91 (D8), 8623–8636.
Rolph, G.D., Stein, A.F., Stunder, B.J.B., 2017. Real-time environmental applications and display sYstem: READY. Environ. Model Softw. 95, 210–228.
Rudnick, R.L., Gao, S., 2003. Composition of Continental Crust. In: Rudnick, R.L., Holland, H.D., Turekian, K.K. (Eds.), Treatise on Geochemistry, pp. 659.
Saltzman, E.S., Savoie, D., Prospero, J.M., Zika, R.G., Mosher, B., 1986. Elevated atmospheric sulfur levels off the Peruvian coast. J. Geophys. Res. 91, 7913–7918.
Salvador, A., Arasa, R., Codina, B., 2016. Aeolian dust forecast in arid and semiarid regions of Peru and Chile and their contribution over particulate matter concentration. J. Geosci. Environ. Prot. 4 (1).
Sanial, V., et al., 2018. Radium-228 as a tracer of dissolved trace element inputs from the Peruvian continental margin. Mar. Chem. 201, 20–34.
Saukel, C., Lamy, F., Stuut, J.-B.W., Tiedemann, R., Vogt, C., 2011. Distribution and provenance of wind-blown SE Pacific surface sediments. Mar. Geol. 280 (1–4), 130–142.
Schlitzer, et al., 2018. The GEOTRACES Intermediate Data Product 2017. Chem. Geo. 493, 210–223.
Shelley, R.U., Morton, P.L., Landing, W.M., 2015. Elemental ratios and enrichment factors in aerosols from the US-GEOTRACES North Atlantic transects. Deep-Sea Res. II Top. Stud. Oceanogr. 116, 262–272.
Shelley, R.U., et al., 2017. Quantification of trace element atmospheric deposition fluxes to the Atlantic Ocean (> 40°N; GEOVIDE, GEOTRACES GA01) during spring 2014. Deep-Sea Res. I Oceanogr. Res. Pap. 119, 34–49.
Sholkovitz, E.R., Sedwick, P.N., Church, T.M., Baker, A.R., Powell, C.F., 2012. Fractional solubility of aerosol iron: synthesis of a global-scale data set. Geochim. Cosmochim. Acta 89, 173–189.
Stein, A.F., et al., 2015. NOAA's HYSPLIT atmospheric transport and dispersion modeling system. Bull. Am. Meteorol. Soc. 96 (12), 2059–2077.
Tagliabue, A., et al., 2016. How well do global ocean biogeochemistry models simulate dissolved iron distributions? Glob. Biogeochem. Cycles 30 (2), 149–174.
Tagliabue, A., et al., 2017. The integral role of iron in ocean biogeochemistry. Nature 543 (7643), 51–59.
Taylor, S.R., McLennan, S.M., 1995. The geochemical evolution of continental crust. Rev. Geophys. 33, 241–265.
Twining, B.S., Baines, S.B., 2013. The trace metal composition of marine phytoplankton. Annu. Rev. Mar. Sci. 5, 191–215.
Ulke, A.G., Longo, K.M.a., Freitas, S.R.d., 2011. Biomass burning in South America: transport patterns and impacts. In: Matovic, D. (Ed.), Biomass - Detection, Production and Usage. InTech, Rijeka (pp. Ch. 19).
Vedamati, J., Chan, C., Moffett, J.W., 2015. Distribution of dissolved manganese in the Peruvian upwelling and oxygen minimum zone. Geochim. Cosmochim. Acta 156, 222–240.
Wagener, T., Guieu, C., Losno, R., Bonnet, S., Mahowald, N., 2008. Revisiting atmospheric dust export to the Southern Hemisphere Ocean: Biogeochemical implications. Glob. Biogeochem. Cycles 22 (2) (n/a–n/a).
Wood, R., et al., 2011. The VAMOS Ocean-Cloud-Atmosphere-Land Study Regional Experiment (VOCALS-REx): goals, platforms, and field operations. Atmos. Chem. Phys. 11 (2), 627–654.